Journal of Computational Physics 258 (2014) 856–870

Contents lists available at ScienceDirect

Journal of Computational Physics

www.elsevier.com/locate/jcp

A fast and high-order method for the three-dimensional elastic wave scattering problem

Fanbin Bu [a], Junshan Lin [b,*], Fernando Reitich [c]

[a] KLA-Tencor Corporation, 1 Technology Dr., Milpitas, CA 95035, USA
[b] Department of Mathematics and Statistics, Auburn University, Auburn, AL 36849, USA
[c] School of Mathematics, University of Minnesota, Minneapolis, MN 55455, USA

ARTICLE INFO

Article history:
Received 2 April 2013
Received in revised form 27 October 2013
Accepted 11 November 2013
Available online 18 November 2013

Keywords:
Boundary integral equation method
Elastic wave scattering
FFT

ABSTRACT

In this paper we present a fast and high-order boundary integral equation method for the elastic scattering by three-dimensional large penetrable obstacles. The algorithm extends the method introduced in [5] for the acoustic surface scattering to the fully elastic case. In our algorithm, high-order accuracy is achieved through the use of the partition of unity and a semi-classical treatment of relevant singular integrals. The computational efficiency associated with the nonsingular integrals is attained by the method of equivalent source representations on a Cartesian grid and Fast Fourier Transform (FFT). The resulting algorithm computes one matrix–vector product associated with the discretization of the integral equation with $O(N^{4/3}\log N)$ operations, and it shows algebraic convergence. Several numerical experiments are provided to demonstrate the efficiency of the method.

1. Introduction

Elastic wave scattering plays a significant role in engineering and industrial design and identification. Examples include the recovery of elastic properties of materials and composites, non-destructive testing and geophysical exploration. In this paper, we consider the elastic wave scattering of a time harmonic (with $e^{i\omega t}$ time dependence) incident wave field that impinges on a penetrable obstacle. In particular, we are interested in the case when the size of the obstacle is several dozen times larger than the wavelength of the incident field. Such scattering problems usually exist in seismic exploration, where the domain of interest is usually several kilometers [4], or in elastography for medical imaging, where the size of human tissue is much larger than the wavelength of the high frequency incident beams [10,11]. Accurate numerical solution of such problems is still challenging nowadays, as the wave field is usually highly oscillatory, and in general it requires a large number of grid points to resolve the wave field with sufficient accuracy.

In the past few decades, various advanced numerical simulators have been developed to model the elastic wave scattering, these include the standard finite difference methods (e.g. [17,20,23,27,31,37]), and finite element methods (e.g. [15,16,19,24,32,35]). However, both of them involve discretization over the volume of the obstacle, and their cost even at moderate frequencies quickly becomes prohibitive. Moreover, the infinite exterior domain has to be truncated into a finite one, and an absorbing boundary condition [9] or perfectly matched layer (PML) [3] needs to be imposed on the boundary. Integral equation formulations, on the other hand, offer some advantages from a numerical perspective. Indeed, compared to the finite element or finite difference approaches, the integral equations are only discretized on the surface of the obstacle, which results in a dramatic reduction of computational cost for a given accuracy. Moreover, they enforce the radiation condition automatically, as the very formulation encodes the correct behavior of outgoing waves. We refer the readers

* Corresponding author.
E-mail addresses: fanbinbu@gmail.com (F. Bu), jzl0097@auburn.edu (J. Lin), reitich@math.umn.edu (F. Reitich).

0021-9991/$ – see front matter
http://dx.doi.org/10.1016/j.jcp.2013.11.009

to [1,14,21,22,26,28] and references therein for recent developments of boundary element methods for solving the elastic scattering problem.

Although the integral formulations provide significant gains in memory requirements, a brute-force integration scheme would lead to $O(N^2)$ computation cost for each matrix–vector product, where N is the number of grid points. This is still formidable even for supercomputers when N is very large. For this reason, a number of algorithms have been introduced to evaluate the discretized integral equations in a fast way, of which the most celebrated algorithm is the fast multipole methods (FMM) [8,25,29,33,36]. The method provides significant gains in computation time with $O(N\log N)$ operations only. However, it also presents certain limitations, such as low-order accuracy. It is shown that the relative error for the numerical solution may be several percent even for the simplest scatterers (see, for example, [7,34]). Moreover, in the elastic wave scattering, multiple-tree frames are needed due to the existence of both longitudinal and transverse waves with different wave speeds in one medium. This results in a nonuniform definition for well-separated groups and greatly complicates the implementation. We refer the readers to [36] for more details in this regard.

The goal of this paper is to present an accurate and efficient boundary integral equation method to solve elastic scattering by large obstacles. A partition of unity and a semi-classical method is employed to evaluate the singular integrals accurately. Nonsingular integrals are evaluated by high-order quadrature rules with a fast method, wherein each matrix–vector product is evaluated with $O(N^{4/3}\log N)$ operations. Our acceleration strategy is based on the two face equivalent source approximation, which reduces the evaluation of nonadjacent interactions in the integral formulations to an evaluation of 3-D Fast Fourier Transform (FFT). It is a nontrivial extension of the acoustic solver in [5] to allow for the evaluation of the elastic wave scattering in three dimensions. It should be mentioned that additional difficulties arise in the context of the elastic wave scattering, since compared to the scalar acoustic wave scattering, the vector elastic wave field consists of a longitudinal and a transverse part propagating at different speeds. Moreover, due to the essential differences in the singularity of Green's tensors, instead of dealing with integrals with weakly singular kernels only, here we have to evaluate integrals with singular and even hypersingular kernels. The resulting fast high-order method attains the accuracy of traditional boundary element method with a significant lower computational cost, especially when N is large. It is capable of handling a wide variety of complex large obstacles. In addition, the equivalent sources are solved independently within each small subdomain, which makes the algorithm suitable for parallelism.

The rest of the paper is organized as follows. Section 2 introduces the mathematical model for the elastic wave scattering problem, and formulates the boundary integral equations. The numerical method is presented in Section 3, where accurate evaluation of singular integrals and acceleration for the far interactions of integrations are discussed in details. We show various numerical results in Section 4 to demonstrate the efficiency of the method, and conclude with some remarks in Section 5.

2. Problem formulation and boundary integral equations

Let Ω_1 denote the body of the obstacle, and $\Omega_2=\mathbb{R}^3\backslash\bar{\Omega}_1$ be its exterior region. The Lamé constants for the regions inside and outside the obstacle are γ_i and μ_i $(i=1,2)$ respectively, and the densities are ρ_i $(i=1,2)$. Assume that an incident wave field $\mathbf{u}^{inc}$ impinges on the obstacle Ω_1. The displacement of the scattered wave and that of the wave excited inside the obstacle satisfy the following elastic wave equations in the frequency domain

$$\frac{1}{k_{p,i}^2}\nabla\nabla\cdot\mathbf{u}_i-\frac{1}{k_{s,i}^2}\nabla\times\nabla\times\mathbf{u}_i+\mathbf{u}_i=0,\quad x\in\Omega_i,\ i=1,2. \tag{2.1}$$

Here $k_{p,i}=\frac{\omega}{c_{p,i}}$ and $k_{s,i}=\frac{\omega}{c_{s,i}}$ are wavenumbers for the longitudinal wave (P-wave) and the transverse wave (S-wave) inside and outside Ω_1, respectively. ω is the operating frequency of the elastic wave, and the wave speeds are given by

$$c_{p,i}=\sqrt{\frac{\gamma_i+2\mu_i}{\rho_i}}\quad\text{and}\quad c_{s,i}=\sqrt{\frac{\mu_i}{\rho_i}},\quad i=1,2.$$

Across the surface Γ of the obstacle, the displacement $\mathbf{u}$ and the traction field $\mathbf{t}$ are continuous. That is,

$$\mathbf{u}_1=\mathbf{u}_2+\mathbf{u}^{inc},\qquad \mathbf{t}_1=\mathbf{t}_2+\mathbf{t}^{inc}\quad\text{on }\Gamma. \tag{2.2}$$

Here the traction field is given by $\mathbf{t}_i=\gamma(\nabla_y\cdot\mathbf{u}_i(x,y))\mathbb{I}+\mu(\nabla_y\mathbf{u}_i(x,y)+\nabla_y\mathbf{u}_i^T(x,y))\cdot\mathbf{n}(y)$ $(i=1,2)$. $\mathbb{I}$ is the identity matrix, and $\mathbf{n}$ is unit outward normal to the surface Γ. The definition for $\mathbf{t}^{inc}$ follows a similar fashion.

At infinity, the scattered wave $\mathbf{u}_2$ satisfies the Sommerfeld radiation condition. More precisely, the displacement $\mathbf{u}_2$ admits the Helmholtz decomposition

$$\mathbf{u}_2=\nabla\phi+\nabla\times\boldsymbol{\psi}, \tag{2.3}$$

where ϕ and $\boldsymbol{\psi}$ satisfy the following radiation conditions:

$$\lim_{r\to\infty}r\left(\frac{\partial\phi}{\partial r}-\mathrm{i}k_{p,2}\boldsymbol{\phi}\right)=0; \tag{2.4}$$

$$\lim_{r\to\infty} r\left(\nabla\times\boldsymbol{\psi}\times\frac{x}{|x|}-\mathrm{i}k_{s,2}\boldsymbol{\psi}\right)=0,\quad r=|x|. \tag{2.5}$$

For simplicity, here we assume the incident wave field is plane wave represented by

$$\mathbf{u}^{inc}=\hat{d}e^{\mathrm{i}k_{p,2}\hat{d}\cdot x}+\hat{d}^{\perp}e^{\mathrm{i}k_{s,2}\hat{d}\cdot x},$$

where $\hat{d}$ is unit wave vector, and $\hat{d}^{\perp}$ is a vector perpendicular to $\hat{d}$. It is obvious that $\mathbf{u}^{inc}$ is the solution of the elastic wave equation in $\mathbb{R}^3$ with the wavenumbers $k_p=k_{p,2}$ and $k_s=k_{s,2}$.

Next we derive the boundary integral equations for the scattering problem (2.1)–(2.5). Let the dyadic Green function $\mathbb{G}_i(x,y)$ for the elastic wave equation satisfy

$$\frac{1}{k_{p,i}^2}\nabla\nabla\cdot\mathbb{G}_i(x,y)-\frac{1}{k_{s,i}^2}\nabla\times\nabla\times\mathbb{G}_i(x,y)+\mathbb{G}_i(x,y)=-\delta(x-y)\mathbb{I}.$$

Then each component of $\mathbb{G}_i(x,y)$ may be expressed as

$$g_i^{jl}(x,y)=\frac{1}{\rho_i\omega^2}\left\{\delta_{jl}k_{s,i}^2g(k_{s,i};x-y)+\partial_j\partial_l\left[g(k_{s,i};x,y)-g(k_{p,i};x-y)\right]\right\},$$

where

$$g(k;x-y)=\frac{1}{4\pi|x-y|}e^{\mathrm{i}k|x-y|}$$

is the Green's function for the scalar Helmholtz equation in $\mathbb{R}^3$, and δ_{jl} is the Kronecker delta.

Let $\bar{\Sigma}_i(x,y)=\gamma(\nabla_y\cdot\mathbb{G}_i(x,y))\mathbb{I}+\mu(\nabla_y\mathbb{G}_i(x,y)+\nabla_y\mathbb{G}_i^T(x,y))$ be the third rank Green tensor [26]. Then the Green tensor for the traction $\mathbb{T}_i(x,y)=\bar{\Sigma}_i(x,y)\cdot\mathbf{n}(y)$, where $\mathbf{n}$ is unit outward normal to the boundary of the obstacle. By Somigliana's identity [28], the excited field $\mathbf{u}_1$ inside the obstacle, the scattered field $\mathbf{u}_2$, and the incident field $\mathbf{u}^{inc}$ satisfy the following integral equations

$$-\frac{1}{2}\mathbf{u}_1(x)=\int_{\Gamma}\mathbb{T}_1(x,y)\mathbf{u}_1(y)-\mathbb{G}_1(x,y)\mathbf{t}_1(y)\,ds_y,\quad x\in\Gamma; \tag{2.6}$$

$$\frac{1}{2}\mathbf{u}_2(x)=\int_{\Gamma}\mathbb{T}_2(x,y)\mathbf{u}_2(y)-\mathbb{G}_2(x,y)\mathbf{t}_2(y)\,ds_y,\quad x\in\Gamma; \tag{2.7}$$

$$-\frac{1}{2}\mathbf{u}^{inc}(x)=\int_{\Gamma}\mathbb{T}_2(x,y)\mathbf{u}^{inc}(y)-\mathbb{G}_2(x,y)\mathbf{t}^{inc}(y)\,ds_y,\quad x\in\Gamma. \tag{2.8}$$

(2.7) + (2.8) yields

$$\frac{1}{2}\mathbf{u}_2(x)-\frac{1}{2}\mathbf{u}^{inc}(x)=\int_{\Gamma}\mathbb{T}_2(x,y)\big(\mathbf{u}_2(y)+\mathbf{u}^{inc}(y)\big)-\mathbb{G}_2(x,y)\big(\mathbf{t}_2(y)+\mathbf{t}^{inc}(y)\big)\,ds_y. \tag{2.9}$$

By subtracting (2.9) from (2.6), and using the continuity conditions

$$\mathbf{u}_1=\mathbf{u}_2+\mathbf{u}^{inc}\quad\text{and}\quad\mathbf{t}_1=\mathbf{t}_2+\mathbf{t}^{inc},$$

it follows that

$$\mathbf{u}(x)+\int_{\Gamma}\big(\mathbb{T}_1(x,y)-\mathbb{T}_2(x,y)\big)\mathbf{u}(y)-\big(\mathbb{G}_1(x,y)-\mathbb{G}_2(x,y)\big)\mathbf{t}(y)\,ds_y=\mathbf{u}^{inc}(x),\quad x\in\Gamma, \tag{2.10}$$

where $\mathbf{u}$ and $\mathbf{t}$ in the equation are the total displacement and traction on Γ. Let

$$\mathbb{W}_i(x,y)=\left[\gamma\big(\nabla_x\cdot\mathbb{G}_i(x,y)\big)\mathbb{I}+\mu\big(\nabla_x\mathbb{G}_i(x,y)+\nabla_x\mathbb{G}_i^T(x,y)\big)\right]\cdot\mathbf{n}(x)$$

and

$$\mathbb{V}_i(x,y)=\left[\gamma\big(\nabla_x\cdot\mathbb{T}_i(x,y)\big)\mathbb{I}+\mu\big(\nabla_x\mathbb{T}_i(x,y)+\nabla_x\mathbb{T}_i^T(x,y)\big)\right]\cdot\mathbf{n}(x).$$

Then the integral equation for the traction field is

$$\mathbf{t}(x)+\int_{\Gamma}\big(\mathbb{V}_1(x,y)-\mathbb{V}_2(x,y)\big)\mathbf{u}(y)-\big(\mathbb{W}_1(x,y)-\mathbb{W}_2(x,y)\big)\mathbf{t}(y)\,ds_y=\mathbf{t}^{inc}(x),\quad x\in\Gamma. \tag{2.11}$$

For brevity, we introduce the following integral operators on Γ:

$$\mathcal{S}_i\boldsymbol{\psi}(x)=\int_{\Gamma}\mathbb{G}_i(x,y)\boldsymbol{\psi}(y)\,ds_y,$$

$$\mathcal{D}_i\boldsymbol{\psi}(x)=\int_{\Gamma}\mathbb{T}_i(x,y)\boldsymbol{\psi}(y)\,ds_y,$$

$$\mathcal{K}_i\boldsymbol{\psi}(x)=\int_{\Gamma}\mathbb{W}_i(x,y)\boldsymbol{\psi}(y)\,ds_y,$$

$$\mathcal{N}_i\boldsymbol{\psi}(x)=\int_{\Gamma}\mathbb{V}_i(x,y)\boldsymbol{\psi}(y)\,ds_y.$$

Define

$$\mathcal{S}=\mathcal{S}_1-\mathcal{S}_2,\qquad \mathcal{D}=\mathcal{D}_1-\mathcal{D}_2,\qquad \mathcal{K}=\mathcal{K}_1-\mathcal{K}_2,\qquad \mathcal{N}=\mathcal{N}_1-\mathcal{N}_2$$

as the difference of two integral operators with associated kernels. From (2.10)–(2.11), we see that the solution of the elastic wave scattering problem (2.1)–(2.5) is reduced to finding a pair $(\mathbf{u},\mathbf{t})$ that solves the following system of integral equations

$$\begin{bmatrix}\mathbf{u}\\ \mathbf{t}\end{bmatrix}+\begin{pmatrix}\mathcal{D} & -\mathcal{S}\\ \mathcal{N} & -\mathcal{K}\end{pmatrix}\begin{bmatrix}\mathbf{u}\\ \mathbf{t}\end{bmatrix}=\begin{bmatrix}\mathbf{u}^{inc}\\ \mathbf{t}^{inc}\end{bmatrix}. \tag{2.12}$$

Similar equations for the scalar problem have been widely used in the acoustic wave propagation, see, for example, [18]. It should be noted that, in the above integral equations, the kernel of the integral operator $\mathcal{S}$ is weakly singular, and $\mathcal{S}$ is a compact operator from $(L^2(\Gamma))^3\to(L^2(\Gamma))^3$. While the kernels of $\mathcal{D}$ and $\mathcal{K}$ are strongly singular, and the kernel of $\mathcal{N}$ is hypersingular. As a consequence, the integral operators $\mathcal{D}$, $\mathcal{K}$ and $\mathcal{N}$ are not compact. The corresponding integral exists in the sense of the Cauchy principle value and the Hadamard finite part respectively.

3. Accurate and efficient evaluations of integrals

3.1. Partition of unity, cubic cells and decomposition of integrals

Following the ideas in [5], we introduce a partition of unity (POU) to reduce the integration over the surface Γ to evaluation of integrals for smooth functions that are compactly supported in the planar sets.

The surface of the obstacle Γ is covered by a number of overlapping patches $\{\mathcal{P}_m\}_{m=1}^{M}$, where each patch $\mathcal{P}_m$ is the image of an open set $\mathcal{H}_m\subset\mathbb{R}^2$ by a smooth invertible mapping ζ_m. A partition of unity subordinated to this covering is chosen such that

$$\sum_{m=1}^{M}w_m(x)=1\quad\text{and each } w_m(x) \text{ is smooth and vanishes outside the patch } \mathcal{P}_m.$$

For a grid point x on Γ, we define an index set that counts all the patch $\mathcal{P}_m$ containing x:

$$\mathcal{M}_x:=\{m\mid x\in\mathcal{P}_m\}.$$

Obviously if x belongs to a region where several patches overlap, the set $\mathcal{M}_x$ has more than one element.

To accommodate the acceleration strategy, we introduce a cubic cell $\mathcal{C}$ that contains the obstacle Ω_1. The cubic $\mathcal{C}$ is decomposed into small identical cubic cells c_{jkl} $(j,k,l=1,2,\ldots,L)$ such that there are L cells along each direction, where the subscript jkl uniquely identifies each cell. The number L is to be determined to guarantee an optimal computational cost for the algorithm. Hence, there is a total of L^3 cubic cells. Most of cubic cells do not contain any discretization points on the surface Γ. Indeed, the number of those that are not empty is approximately $O(L^2)$. It can also be counted that each of those nonempty cells contains approximately $O(\frac{N}{L^2})$ grid points of Γ, where N is total number of grid points on Γ.

Next we give precise definition of adjacency. For a space point x belonging to some cell c_{j_0,k_0,l_0}, define a set

$$\mathcal{A}_x:=\big\{y\;\big|\;y\in c_{jkl},\ |j-j_0|\leqslant 1,\ |k-k_0|\leqslant 1,\ |l-l_0|\leqslant 1\big\}$$

that contains c_{j_0,k_0,l_0} and its 26 neighboring cells. Then two points x and y are called adjacent if $y\in\mathcal{A}_x$, and nonadjacent if otherwise.

Let $\mathbb{K}(x, y)$ denote a generic integral kernel, which can be $\mathbb{G}_i(x, y)$, $\mathbb{T}_i(x, y)$, $\mathbb{W}_i(x, y)$ or $\mathbb{V}_i(x, y)$, and $\boldsymbol{\psi}$ be the corresponding potential density function, which is the displacement $\mathbf{u}$ or the traction field $\mathbb{T}$. Then the evaluation of each integral in (2.12) on each patch can be decomposed as adjacent and nonadjacent interactions:

$$\int_{\Gamma} \mathbb{K}(x, y)\boldsymbol{\psi}(y)\, ds_y = \sum_{m=1}^{M} \int_{\mathcal{P}_m} \mathbb{K}(x, y)\boldsymbol{\psi}(y) w_m(y)\, ds_y = \sum_{m=1}^{M} \Bigg(\int_{\mathcal{P}_m \cap \mathcal{A}_x} + \int_{\mathcal{P}_m \cap \mathcal{A}_x^c} \Bigg) \mathbb{K}(x, y)\boldsymbol{\psi}(y) w_m(y)\, ds_y,$$

where $\mathcal{A}_x^c$ denotes the complement of the adjacent set $\mathcal{A}_x$. Furthermore, the adjacent interactions in the above formula can be written as the sum of integrals over patches containing the target point x and those not containing x:

$$\Bigg(\sum_{m \in \mathcal{M}_x} + \sum_{m \notin \mathcal{M}_x} \Bigg) \int_{\mathcal{P}_m \cap \mathcal{A}_x} \mathbb{K}(x, y)\boldsymbol{\psi}(y) w_m(y)\, ds_y.$$

Therefore, the whole integral is decomposed into three separate parts:

$$\sum_{m \notin \mathcal{M}_x} \int_{\mathcal{P}_m \cap \mathcal{A}_x} \cdots + \sum_{m \in \mathcal{M}_x} \int_{\mathcal{P}_m \cap \mathcal{A}_x} \cdots + \sum_{m=1}^{M} \int_{\mathcal{P}_m \cap \mathcal{A}_x^c} \cdots. \tag{3.13}$$

In the first part of (3.13), the target point x and the source point y are not in the same patch $\mathcal{P}_m$, hence the integral kernel $\mathbb{K}(x, y)$ remains nonsingular within the patch. Moreover, the integrand vanishes to high order at the boundary. Therefore, the trapezoidal rule is a quadrature with super-algebraic convergence for such an integrand. In this case, x and y are adjacent, thus the computational cost for the integration is very low. In light of the fact that there is $O(\frac{N}{L^2})$ grid points inside each cell, the operations for all the target points x is $O(\frac{N^2}{L^2})$.

The second part of (3.13) is a singular integral. The kernels $\mathbb{K}(x, y)$ can be weakly singular, strongly singular, or even hypersingular. An accurate evaluation of those singular integrals is necessary to guarantee a high-order scheme for the whole integration. The evaluation process is discussed in details in Section 3.2. Similar to the first part, this adjacent interactions also requires $O(\frac{N^2}{L^2})$ operations.

The last part of (3.13) is nonadjacent nonsingular interactions. Therefore, high-order accuracy can be retained by the trapezoidal rule. However, a direct use of such an integrator would lead to a $O(N^2)$ algorithm. We adopt the idea of equivalent sources representation and present an acceleration strategy with a computational cost of $O(NL \log N + \frac{N^2}{L^2})$ in Section 3.3.

The integrations for the above three parts complete the whole matrix vector product for a discretized version of the integral equation system (2.12). It is obvious that this high-order method requires $O(NL \log N + \frac{N^2}{L^2})$ operations in total. By choosing $L = O(N^{1/3})$, the accelerated algorithm is obtained with a computation cost of $O(N^{4/3} \log N)$.

3.2. Singular integration

Note that a smooth invertible mapping ζ_m maps an open set $\mathcal{H}_m \subset \mathbb{R}^2$ to each patch $\mathcal{P}_m$. Let $x = \zeta_m(u_0, v_0)$, $y = \zeta_m(u, v)$, then the singular integral of (3.13) over $\mathcal{P}_m$ can be rewritten as an integral over a subset of $\mathcal{H}_m$:

$$\int_{\mathcal{P}_m \cap \mathcal{A}_x} \mathbb{K}(x, y)\boldsymbol{\psi}(y) w_m(y)\, ds_y = \int_{\tilde{\mathcal{H}}_m} \mathbb{K}\big(\zeta_m(u_0, v_0), \zeta_m(u, v)\big)\boldsymbol{\phi}\big(\zeta_m(u, v)\big) J(u, v)\, du\, dv, \tag{3.14}$$

where

$$\tilde{\mathcal{H}}_m = \big\{(u, v) \in \mathcal{H}_m \,\big|\, \zeta_m(u, v) \in \mathcal{P}_m \cap \mathcal{A}_x\big\},$$

$\boldsymbol{\phi}(\zeta_m(u, v)) = \boldsymbol{\psi}(\zeta_m(u, v)) w_m(\zeta_m(u, v))$, and $J(u, v)$ is the Jacobian.

We introduce a floating partition of unity to localize the singularity. To be more precise, let the smooth function $\eta(r) = 1$ if the distance between (u_0, v_0) and (u, v) is less than r_0 and vanishes if the distance is greater than or equal to r_1. The pair η and $1 - \eta$ forms a partition of unity in the neighborhood of x, by which (3.14) can be decomposed into a singular part and a nonsingular part in the following way:

$$\int_{\tilde{\mathcal{H}}_m} \mathbb{K}\big(\zeta_m(u_0, v_0), \zeta_m(u, v)\big)\boldsymbol{\phi}\big(\zeta_m(u, v)\big) J(u, v)\eta\, du\, dv + \int_{\tilde{\mathcal{H}}_m} \mathbb{K}\big(\zeta_m(u_0, v_0), \zeta_m(u, v)\big)\boldsymbol{\phi}\big(\zeta_m(u, v)\big) J(u, v)(1 - \eta)\, du\, dv.$$

The second integral is adjacent nonsingular interactions, since $1-\eta$ vanishes in the vicinity of x. Therefore, again the integral may be evaluated accurately by the trapezoidal rule. The first integral, on the other hand, contains singular kernels, and is treated by a semi-classical method introduced in [13]. We now describe the method for the above singular integral as follows. The readers are also referred to [6] for the treatment of singular integrals in the case of scattering by infinitely thin screens.

Define the local polar coordinate

$$u = u_0 + \rho\cos\theta, \tag{3.15}$$

$$v = v_0 + \rho\sin\theta. \tag{3.16}$$

Let

$$\mathbf{F}(u,v) = \mathbb{K}\big(\zeta_m(u_0,v_0),\zeta_m(u,v)\big)\boldsymbol{\phi}\big(\zeta_m(u,v)\big)J(u,v)\eta$$

and

$$\tilde{\mathbf{F}}(\rho,\theta) = \mathbf{F}(u_0+\rho\cos\theta, v_0+\rho\sin\theta)\rho.$$

Then the singular integral in the polar coordinate takes the form of

$$\int_0^{r_1}\int_0^{2\pi} \tilde{\mathbf{F}}(\rho,\theta)\,d\theta\,d\rho. \tag{3.17}$$

The integrand $\tilde{\mathbf{F}}(\rho,\theta)$ adopts a Laurent series expansion with respect to ρ:

$$\tilde{\mathbf{F}}(\rho,\theta) = \frac{\tilde{\mathbf{F}}_{-2}(\theta)}{\rho^2} + \frac{\tilde{\mathbf{F}}_{-1}(\theta)}{\rho} + O(1). \tag{3.18}$$

For weakly singular kernels, that is when $\mathbb{K}(x,y) = \mathbb{G}_i(x,y)$, we have $\tilde{\mathbf{F}}_{-2}(\theta) = \tilde{\mathbf{F}}_{-1}(\theta) = 0$. When $\mathbb{K}(x,y) = \mathbb{T}_i(x,y)$ or $\mathbb{K}(x,y) = \mathbb{W}_i(x,y)$, it is a singular kernel and $\tilde{\mathbf{F}}_{-2}(\theta) = 0$. For hypersingular kernels $\mathbb{V}_i(x,y)$, both $\tilde{\mathbf{F}}_{-2}(\theta)$ and $\tilde{\mathbf{F}}_{-1}(\theta)$ do not vanish. The explicit expressions of $\tilde{\mathbf{F}}_{-2}(\theta)$ and $\tilde{\mathbf{F}}_{-1}(\theta)$ corresponding to different Green tensors are derived in Appendix A.

In this way, we obtain the following formula to evaluate the singular integral:

$$\int_0^{r_1}\int_0^{2\pi} \tilde{\mathbf{F}}(\rho,\theta)\,d\theta\,d\rho = \mathcal{I}_0 + \mathcal{I}_{-1} + \mathcal{I}_{-2},$$

where the regular part

$$\mathcal{I}_0 = \int_0^{r_1}\int_0^{2\pi} \tilde{\mathbf{F}}(\rho,\theta) - \frac{\tilde{\mathbf{F}}_{-1}(\theta)}{\rho} - \frac{\tilde{\mathbf{F}}_{-2}(\theta)}{\rho^2}\,d\theta\,d\rho,$$

and the singular parts

$$\mathcal{I}_{-1} = \int_0^{r_1}\int_0^{2\pi} \frac{\tilde{\mathbf{F}}_{-1}(\theta)}{\rho}\,d\theta\,d\rho;$$

$$\mathcal{I}_{-2} = \int_0^{r_1}\int_0^{2\pi} \frac{\tilde{\mathbf{F}}_{-2}(\theta)}{\rho^2}\,d\theta\,d\rho.$$

Here the singular integrals $\mathcal{I}_{-1}$ and $\mathcal{I}_{-2}$ are understood in the sense of Cauchy principle value and Hadamard finite part sense respectively. In fact, by noting that $\tilde{\mathbf{F}}_{-1}(\theta) = -\tilde{\mathbf{F}}_{-1}(\theta+\pi)$ (see Appendix A, Lemma A.1), we have $\mathcal{I}_{-1} = 0$. On the other hand, a direct calculation yields

$$\mathcal{I}_{-2} = -\frac{1}{r_1}\int_0^{2\pi} \tilde{\mathbf{F}}_{-2}(\theta)\,d\theta.$$

The regular part $\mathcal{I}_0$ is smooth, hence it may be evaluated accurately by Gaussian quadratures.

Note that the values of density function $\boldsymbol{\phi}$ are known only on the Cartesian grid points in each patch, and its values on radial quadrature points of $\mathcal{I}_0$ are not known. To obtain the function values at those radial integration point, the following standard fast interpolation process is applied:

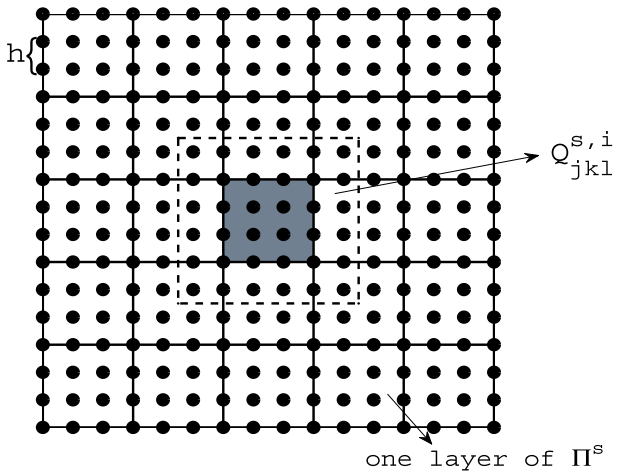

Fig. 1. Cartesian grid points on one layer of Π^s, and equivalent source points for cell c_{jkl} on the face (gray square) parallel to $x_s = 0$. The dashed square containing the cell face is $\mathcal{Q}^{s,i}_{jkl}$ $(i = 1, 2)$.

1. Based on the function values on the Cartesian grid points, obtain the Fourier coefficients of $\boldsymbol{\phi}$ along the grid lines via FFT.
2. Evaluate the function values and its derivatives on a refined grid via FFT.
3. Construct a cubic interpolating polynomial on each interval of the refined grid using the values obtained in 2.

This process yields accurate interpolations by cubic splines and it only contributes a negligible amount of computation cost.

3.3. Fast nonsingular integration

The fast evaluation of the nonadjacent nonsingular interactions in (3.13) is based on the so-called equivalent source representations. In fact, let $\mathbb{G}(x, y) = \mathbb{G}_i(x, y)$ and $\mathbb{T}(x, y) = \mathbb{T}_i(x, y)$, then the discretized version of the nonsingular integral

$$\sum_{m=1}^{M} \int_{\mathcal{P}_m \cap \mathcal{A}_x^c} \mathbb{T}(x, y)\mathbf{u}(y)w_m(y) - \mathbb{G}(x, y)\mathbf{t}(y)w_m(y)\, ds_y \tag{3.19}$$

can be viewed as a potential due to some monopoles and dipoles located on the grid points, which we refer to as "true sources". For each cubic cell c_{jkl}, the field radiated by the true sources inside c_{jkl} can be approximated by the field radiated by equivalent sources located on two parallel faces of c_{jkl}.

We use three independent sets of equivalent sources. Let us introduce Cartesian grid points on each face of cubic cell c_{jkl} and for all cells, with an identical grid size h. Let Π^s $(s = 1, 2, 3)$ be the set of all Cartesian grid points with the corresponding cell faces parallel to the plane $x_s = 0$. It is obvious that Π^s lies on $L + 1$ parallel planes (see Fig. 1 for one layer of the Cartesian grid points).

For each cubic cell c_{jkl}, let $\mathcal{Q}^{s,1}_{jkl}$ and $\mathcal{Q}^{s,2}_{jkl}$ be two squares that contain two parallel faces of the cell respectively (see the dashed square in Fig. 1). We define a subset of Cartesian grid points on the parallel faces for cell c_{jkl} by letting

$$\Pi^s_{jkl} = \Pi^s \cap \left(\mathcal{Q}^{s,1}_{jkl} \cup \mathcal{Q}^{s,2}_{jkl}\right). \tag{3.20}$$

In practice, the width of $\mathcal{Q}^{s,1}_{jkl}$ and $\mathcal{Q}^{s,2}_{jkl}$ is equal or larger than the length of the diagonal of the cell faces to guarantee an accurate approximation.

The equivalent sources associated with the cell c_{jkl} are located on the Cartesian grid Π^s_{jkl}, with elastic monopoles as $\boldsymbol{\xi}^s_{jkl,n}$ and dipoles as $\boldsymbol{\sigma}^s_{jkl,n}$ on each grid point $x^s_{jkl,n} \in \Pi^s_{jkl}$ $(n = 1, 2, \ldots, N_{equiv})$. Thus the field generated by these equivalent sources is

$$\boldsymbol{\phi}^{equiv,s}_{jkl}(x) = \sum_{n=1}^{N_{equiv}} \mathbb{G}\left(x, x^s_{jkl,n}\right)\boldsymbol{\xi}^s_{jkl,n} + \mathbb{T}\left(x, x^s_{jkl,n}\right)\boldsymbol{\sigma}^s_{jkl,n}. \tag{3.21}$$

Indeed, $\boldsymbol{\phi}^{equiv,s}_{jkl}$ is an accurate approximation of the field $\boldsymbol{\phi}^{true}_{jkl}$ generated by the true sources associated with the cell as long as x is not adjacent to c_{jkl}. That is, the contribution from each cell in the integral (3.19) can be approximated accurately by the field $\boldsymbol{\phi}^{equiv,s}_{jkl}$ generated by the equivalent sources in (3.21). The accuracy of such approximation is discussed in Section 4.

In order to determine the intensities $\boldsymbol{\xi}^s_{jkl,n}$ and $\boldsymbol{\sigma}^s_{jkl,n}$, a least square solution for the following overdetermined linear system is solved

$$\mathbb{P}\begin{bmatrix}\boldsymbol{\xi}\\ \boldsymbol{\sigma}\end{bmatrix} = \mathbf{b}, \tag{3.22}$$

where the $n^{coll} \times N^{equiv}$ matrix $\mathbb{P}$ corresponds to the evaluation of $\boldsymbol{\phi}^{equiv}_{jkl}$ at n^{coll} collocation points located at the boundary of the adjacent set $\mathcal{A}_x$, and the vector $\mathbf{b}$ is the field $\boldsymbol{\phi}^{true}_{jkl}$ at collocation points generated by true sources. Note that, since all the cells are identical, the QR decomposition of $\mathbb{P}$ need only be computed once and stored for repeated use.

Now the evaluation of the nonadjacent interactions (3.19) for each grid point $x \in \Pi^s$ is equivalent to the convolution like (3.21) on the whole Cartesian girds Π^s subtracted by the contributions from adjacent cells. To be more precise,

$$\boldsymbol{\phi}^{equiv,s} = \boldsymbol{\phi}^{equiv,s}_{total} - \boldsymbol{\phi}^{equiv,s}_{adj},$$

where the convolution on the whole Cartesian girds Π^s is given by

$$\boldsymbol{\phi}^{equiv,s}_{total} = \sum_{y\in\Pi^s} \mathbb{G}(x,y)\boldsymbol{\xi}^s_y + \mathbb{T}(x,y)\boldsymbol{\sigma}^s_y, \tag{3.23}$$

$\boldsymbol{\xi}^s_y$ and $\boldsymbol{\sigma}^s_y$ is the sum of all elastic monopole and dipole intensities located at y respectively, and

$$\boldsymbol{\phi}^{equiv,s}_{adj} = \sum_{c_{jkl}\ \text{adjacent to}\ x} \boldsymbol{\phi}^{equiv,s}_{jkl}(x). \tag{3.24}$$

Note that in (3.23) and (3.24), we define $\mathbb{G}(x,y) = \mathbb{T}(x,y) = 0$ if $y = x$. Since both $\boldsymbol{\phi}^{equiv,s}_{total}$ and $\boldsymbol{\phi}^{equiv,s}_{adj}$ are convolutions on a Cartesian grid, they can be evaluated efficiently with FFT. By doing this we obtain $\boldsymbol{\phi}^{equiv,s}$ (or equivalently the nonadjacent interaction (3.19)) on the Cartesian grid points located on the faces of each cell c_{jkl}.

Finally, to obtain the field values at the true source locations inside each cell, a Dirichlet problem for the elastic wave equation is solved. We assume that the size of the cell is chosen such that no resonance is present. Then the problem is uniquely solvable, and the solution admits a plane wave expansion [2,12]:

$$\mathbf{u} = \mathbf{u}_P + \mathbf{u}_{SH} + \mathbf{u}_{SV} = \sum_{j=1}^{N_d}\left(\alpha_{p,j}\hat{d}_j e^{ik_p\hat{d}_j\cdot x} + \alpha_{sh,j}\hat{d}_j^{\perp}\, e^{ik_s\hat{d}_j\cdot x} + \alpha_{sv,j}\left(\hat{d}_j\times\hat{d}_j^{\perp}\right)e^{ik_s\hat{d}_j\cdot x}\right). \tag{3.25}$$

Here $\hat{d}_j$ is the unit wave vector, and $\hat{d}_j^{\perp}$ denotes the vector perpendicular to $\hat{d}_j$. $\alpha_{p,j}$, $\alpha_{sh,j}$ and $\alpha_{sv,j}$ are the coefficients for P-wave, SH-wave and SV-wave respectively. The coefficients are chosen such that the resulting wave field $\mathbf{u}$ matches the wave filed on the boundary of the cell. This also requires solving an over-determined linear system $\mathbb{B}\boldsymbol{\alpha} = \boldsymbol{\phi}_{bnd}$. Again, note that each cell is identical, hence the QR decomposition of $\mathbb{B}$ need only be computed once and stored for repeated use. By evaluating (3.25) on the locations of true sources inside each cell we finally obtain the value of the integral (3.19) for each grid point on the surface Γ.

Similarly, the nonsingular integral

$$\sum_{m=1}^{M}\int_{\mathcal{P}_m\cap\mathcal{A}_x^c} \mathbb{V}_i(x,y)\mathbf{u}(y)w_m(y) - \mathbb{W}_i(x,y)\mathbf{t}(y)w_m(y)\,ds_y$$

can be computed applying the traction operator to the plane wave expansion (3.25):

$$\gamma(\nabla_x\cdot\mathbb{I})\mathbf{u} + \mu\left(\nabla_x\mathbf{u} + \nabla_x\mathbf{u}^T\right)\cdot\mathbf{n}(x),$$

and evaluating inside each cell.

In practice, to achieve sufficient accuracy, the total number M of equivalent sources on each parallel plane is $O(N)$. That is, M is approximately equal to the number of points required by the Nyquist sampling theorem. Now we can calculate the computational cost for the nonadjacent interactions. By noting the fact that the QR decomposition of both P and B are computed ahead and stored for repeated use, then the identification of equivalent sources by (3.22) and obtaining the coefficients for the plane expansion by (3.25) only requires $O(\frac{N^2}{L^2})$ operations. While the convolutions (3.23) by FFT requires $O(NL\log N)$. Therefore, evaluating the nonadjacent interactions is completed with a total computational cost of $O(NL\log N + \frac{N^2}{L^2})$.

Table 1
Relative error ε_2 for different discretizations.

Discretization	Discretization density	ε_2
4 patches $\times$ (24×24)	6 pts per shear wavelength	1.12×10^{-2}
4 patches $\times$ (32×32)	8 pts per shear wavelength	4.22×10^{-3}
4 patches $\times$ (64×64)	16 pts per shear wavelength	1.46×10^{-4}

Table 2
Relative error for equivalent source representations.

N_{equiv}	n_{coll}	N_c	ε_∞
$9 \times 9 \times 2$	602	5×5	8.73×10^{-6}
$12 \times 12 \times 2$	866	6×6	1.29×10^{-7}
$16 \times 16 \times 2$	1538	8×8	3.58×10^{-10}
$20 \times 20 \times 2$	2402	10×10	1.72×10^{-12}

4. Numerical results

We test the accuracy and efficiency of the method by several examples. In all examples, for simplicity the Lamé constants and densities for elastic medium inside and outside the obstacle are given by $\gamma_1 = 0.4$, $\mu_1 = 0.2$, $\rho_1 = 0.8$ and $\gamma_2 = 1.2$, $\mu_2 = 0.2$, $\rho_2 = 0.8$, respectively. Denote the wavelength of P-wave and S-wave by $\lambda_{p,i}$ and $\lambda_{s,i}$ $(i = 1, 2)$. In general the wavelength of P-wave $\lambda_{p,i}$ is larger than that of S-wave $\lambda_{s,i}$. Note that here the Lamé constants are chosen such that the wavelengths for the S-wave are identical in two elastic medium. We introduce a notation λ by letting $\lambda_{s,1} = \lambda_{s,2} = \lambda$.

Example 1 (*Accuracy of numerical solution*). Consider a penetrable ball embedded in an infinite elastic medium. Assume that the incident wave is a longitudinal plane wave that takes the form $\mathbf{u}^{inc} = \hat{d}e^{ik_{p,2}\hat{d}\cdot x}$, where the propagation direction $\hat{d} = (0, 0, -1)^T$.

We consider a ball with radius equal to 2λ. For this case the true solution admits an expansion by spherical harmonics and Bessel functions, and can be evaluated analytically. We refer the reader to [38] for details and the expansion formulas. The numerical solutions are obtained for several different discretizations, and the corresponding near-field errors are shown in Table 1. In the discretization column, the number of patches and the discretization points on each patch are given. To solve the linear system arising from the discretization of (2.12), the GMRES algorithm is applied [30]. By noting the fact that both the displacement $\mathbf{u}$ and the traction field $\mathbf{t}$ are unknown in the system (2.12), the size of the dense matrix resulting from the specified discretization is $6N \times 6N$, where N is the total number of grid points on the surface of the obstacle. The relative L_2-norm error in the near field is defined by

$$\varepsilon_2 = \frac{(\int_{\mathbb{S}} |\mathbf{u_2}^{num} - \mathbf{u_2}^{true}|^2 \, dx)^{1/2}}{(\int_{\mathbb{S}} |\mathbf{u_2}^{true}|^2 \, dx)^{1/2}},$$

where the integral is evaluated over a sphere $\mathbb{S}$ with radius equal to 4λ, and $\mathbf{u_2}^{true}$ is true scattered field evaluated analytically. The study in Table 1 clearly demonstrates the convergence and the high-order accuracy of the presented algorithm.

Example 2 (*Accuracy of equivalent source representation*). In the evaluation of nonsingular nonadjacent interactions, the potential due to true sources is approximated by equivalent sources on two parallel faces of each cell. In this example we demonstrate the accuracy of such approximation. Consider a cell c_{jkl} with a side length of λ. The true sources are uniformly randomly distributed inside the cell with a density of 6 points per wavelength. Hence there is a total of 216 true sources. The equivalent sources are placed on the Cartesian grid Π^1_{jkl} parallel to $x_1 = 0$ (see definition (3.20)). The collocation points are located on the surfaces of a concentric cell with a side length of 3λ. For several different sets of equivalent sources, the accuracy of approximation for the wave field at points not adjacent to the cell c_{jkl} is shown in Table 2.

Here N_{equiv} is the number of equivalent sources on two faces, i.e.,

$$N_{equiv} = \sharp\big(\Pi^s \cap (\mathcal{Q}^{s,1}_{jkl} \cup \mathcal{Q}^{s,2}_{jkl})\big). \tag{4.26}$$

n_{coll} is the number of collocation points, and N_c is the number of equivalent source points lying inside each face of cell c_{jkl}. Note that the equivalent source points lying within each face of the cell is a subset of $\Pi^1_{jkl} \cap \mathcal{Q}^{1,i}_{jkl}$ $(i = 1, 2)$, since the width of the square $\mathcal{Q}^{1,1}_{jkl}$ and $\mathcal{Q}^{1,2}_{jkl}$ containing the cell faces is approximately equal to the length of the diagonal of the cell faces. The relative maximum error ε_∞ is computed on a concentric sphere with a radius of 3λ. 100 realizations of randomly distributed true sources are performed, among which we record the largest maximum error ε_∞. It is seen that with a sampling frequency of 6 equivalent source points in each wavelength, the equivalent source approximation (3.21) is sufficiently accurate.

Table 3
Computational cost for the accelerated and non-accelerated algorithms.

Diameter	Discretization	L	N_{equiv}	n_{coll}	Time/iter. (present)	Time/iter. (no accel.)	Iteration number	ε_2
10λ	$4 \times 64 \times 64$	16	162	602	4.5 min	10.5 min	44	1.09×10^{-2}
20λ	$4 \times 128 \times 128$	32	162	602	19.3 min	2.7 h	103	1.24×10^{-2}
30λ	$4 \times 180 \times 180$	45	162	602	40.3 min	10.4 h	136	1.11×10^{-2}

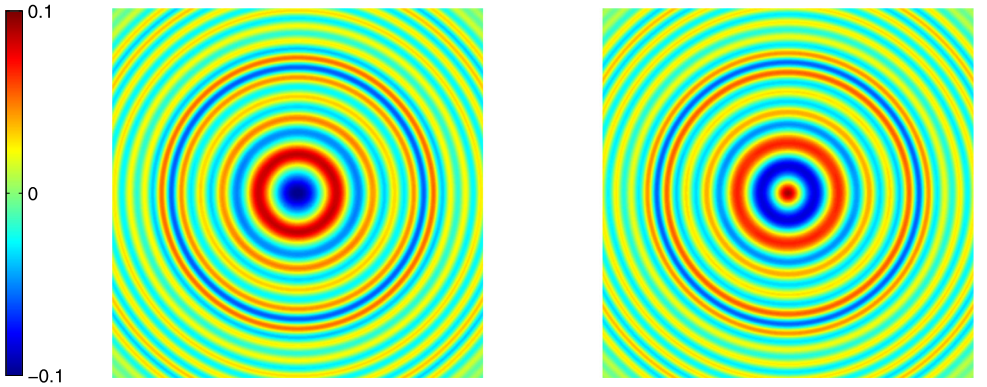

Fig. 2. z component of the scattered field on the plane $x_3 = -30\lambda$ for a spherical obstacle with diameter equal to 30λ. The left figure is the real part, and the right one is the imaginary part.

Table 4
Relative L_2-norm error for different discretizations over a bean type obstacle.

N	Discretization density	ε_2
2304	6 pts per shear wavelength	1.28×10^{-2}
4096	8 pts per shear wavelength	6.37×10^{-3}
16 384	16 pts per shear wavelength	3.15×10^{-4}

Example 3 (*Scattering by large spherical medium*). We consider the scattering by a large penetrable ball with a longitudinal plane wave propagating in negative x_3 direction, and compare the computational cost between the algorithms with and without acceleration. Three different sizes of the obstacle are considered with diameter equal to 10λ, 20λ and 30λ, respectively.

The discretization and acceleration parameters are given in Table 3. Here L is the number of small cells in each direction, and N_{equiv} is the number of equivalent sources on two faces of each cell defined by (4.26). Again in the discretization column, the number of patches and the discretization points on each patch are given. For each case, the discretization density is approximately 6 points in each shear wavelength. The computation is run sequentially on a single processor and the GMRES iteration process is terminated when the residual is reduced by a factor of 10^{-7}. It is seen that the computational cost of the accelerated algorithm is substantially reduced compared to the non-acceleration one. For example, for an obstacle with the size of 30λ and 777 600 unknowns, the accelerated algorithm is approximately 15 times faster than the non-accelerated counterpart. The relative L_2-norm error on a sphere of radius twice as large as the obstacle is also displayed for three cases. For the spherical obstacle with diameter equal to 30λ, we also plot the z component of the scattered field behind the obstacle (on the plane $x_3 = -30\lambda$) in Fig. 2.

Example 4 (*Scattering by obstacle with complex geometry*). In this example, we consider the scattering by a bean type penetrable obstacle shown in Fig. 3. The surface of the obstacle is described by the equation

$$\frac{x_1^2}{R^2} + \frac{(x_2 - \alpha_1 \cos(\pi x_1/R))^2}{R^2(1 - \alpha_2 \cos(\pi x_1/R))} + \frac{x_3^2}{R^2(1 - \alpha_3 \cos(\pi x_1/R))} = 1, \tag{4.27}$$

where $\alpha_1 = 0.2$, $\alpha_1 = 0.4$, and $\alpha_3 = 0.1$. First, we test the accuracy of the method by considering the case when $R = 2\lambda$. The accuracy of the obtained scattered field for different discretizations is shown in Table 4. Here the reference solution is obtained with 40 000 grid points such that the discretization density is approximately 25 points per shear wavelength λ, and the relative L_2-norm error is evaluated over a sphere $\mathbb{S}$ with radius equal to 4λ. It is seen that the algorithm still attains convergence and high-order accuracy for the bean type obstacle.

Next consider a large obstacle by letting $R = 15\lambda$ in (4.27) such that the largest dimension of the obstacle is $2R = 30\lambda$. The incident longitudinal wave again propagates long the negative x_3 direction. We discretize the surface with 129 600 grid

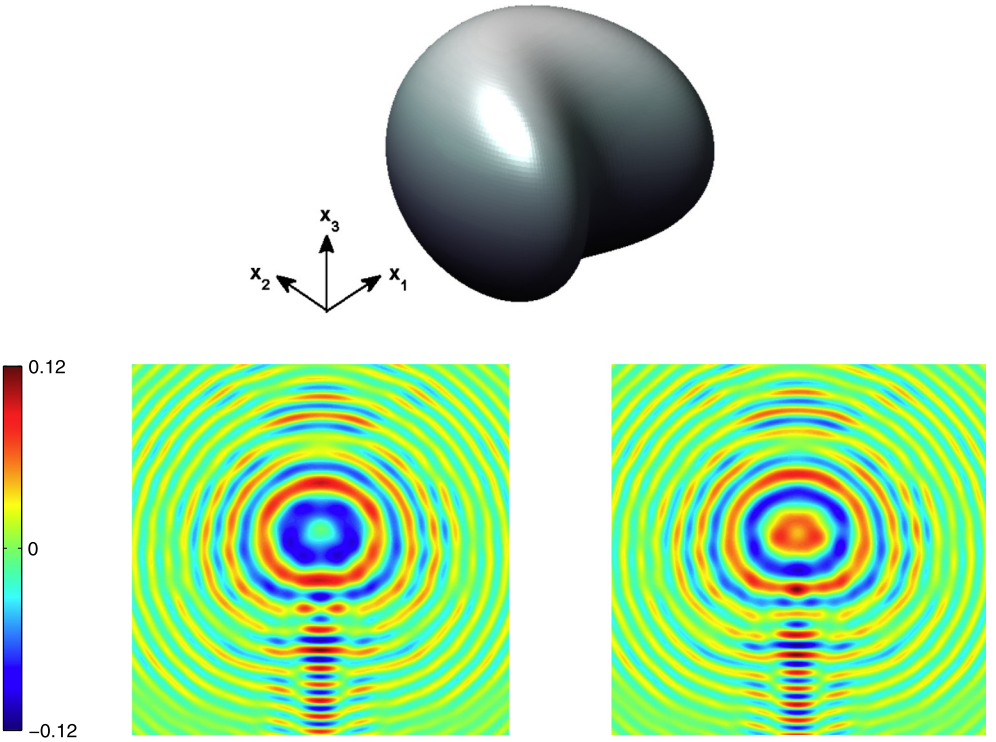

Fig. 3. Bean type obstacle (top), and the x_3 component of the scattered field on the plane $x_3 = -30\lambda$ when $R = 15\lambda$. Real part: bottom left; imaginary part: bottom right.

points, and set the acceleration parameters as $L = 45$ and $N_{equiv} = 162$ respectively. The GRMES iteration is terminated when the residual is reduced by a factor of 10^{-6}, and each iteration takes approximately 46.3 minutes. The resulting scattered field on the plane $x_3 = -30\lambda$ is shown in Fig. 3. It is seen that the multiple scattering effect incurred by the concave portion of the obstacle is accurately captured.

5. Conclusions

A fast method with a computational cost of $O(N^{4/3}\log N)$ for each matrix–vector product is presented for the elastic scattering by large penetrable obstacles. The accelerated algorithm is significantly more efficient than the non-accelerated one, and is capable of dealing with scattering problems with large complicated obstacle within a reasonable time. Numerical results also demonstrate high-order accuracy for the obtained solutions. Future work along this direction is to develop efficient preconditioners for the integral equation solver with an aim to reduce the number of GMRES iterations. This is imperative since in general the number of iterations increases with the size of the obstacle, which is also observed in the numerical examples shown in Section 4. Another direction is to generalize the method to viscoelastic-fluid coupling problems, which has important applications in medical imaging techniques such as ultrasound vibro-acoustography.

Appendix A. Singular parts of Green tensors

For a fixed medium with wavenumbers k_p and k_s for P-wave and S-wave respectively, each component of the traction Green tensor $\mathbb{T}$ can be written explicitly as

$$T_{ij} = \frac{1}{2\pi r^2}\left\{(A_1 r_i r_j + A_2\delta_{ij})r_m n_m^{(y)} + \left(A_2 r_j n_i^{(y)} + A_3 r_i n_j^{(y)}\right)\right\},$$

where

$$r = |y - x|, \qquad r_j = \frac{y_j - x_j}{r}, \qquad \tau = \mathrm{i}k_s r, \qquad \alpha = \frac{k_p}{k_s},$$
$$M(\tau) = \frac{e^{\alpha\tau}(1-\alpha\tau) - e^{\tau}(1-\tau)}{\tau^2}, \qquad \psi = e^{\tau} - M(\tau), \qquad \chi = e^{\alpha\tau}\alpha^2 - e^{\tau} + 3M(\tau),$$

and

$$A_1 = \tau\chi'(\tau) - 3\chi,$$
$$A_2 = \big(\tau\psi'(\tau) - \psi + \chi\big)/2,$$
$$A_3 = \chi + \big(1/(2\alpha^2) - 1\big)(A_1 + 2A_2 + 3\chi).$$

Note that

$$\tilde{\mathbf{F}}(\rho,\theta) = \mathbb{T}\boldsymbol{\phi} J\eta\rho,$$

where $\boldsymbol{\phi}$ is the density, η is the function that localizes the singularity, and J is the Jacobian. To obtain the expression for $\tilde{\mathbf{F}}_{-1}(\theta)$, the Taylor expansion of $y_j - x_j$ is needed:

$$\begin{aligned} y_j - x_j &= \rho\left[\frac{\partial y_j}{\partial u}(u_0,v_0)\cos\theta + \frac{\partial y_j}{\partial v}(u_0,v_0)\sin\theta\right] \\ &\quad + \rho^2\left[\frac{\partial^2 y_j}{\partial u^2}(u_0,v_0)\frac{\cos^2\theta}{2} + \frac{\partial^2 y_j}{\partial u\partial v}(u_0,v_0)\cos\theta\sin\theta + \frac{\partial y_j}{\partial v^2}(u_0,v_0)\frac{\sin^2\theta}{2}\right] + O\big(\rho^3\big) \\ &= \rho C_j(\theta) + \rho^2 D_j(\theta) + O\big(\rho^3\big), \end{aligned} \tag{A.1}$$

where we have introduced notations $C_j(\theta)$ and $D_j(\theta)$ for conciseness. Similarly,

$$r = \rho C(\theta)\left(1 + \rho\frac{E(\theta)}{C^2(\theta)}\right) + O\big(\rho^3\big). \tag{A.2}$$

In the above formula, $C(\theta) = (\sum_{j=1}^3 C_j^2(\theta))^{1/2}$ and $E(\theta) = \sum_{j=1}^3 C_j(\theta)D_j(\theta)$. By combining (A.3) and (A.2), it follows that

$$\frac{y_j - x_j}{r} = \frac{C_j}{C} + \rho\left(\frac{D_j}{C} - \frac{C_j E}{C^3}\right) + O\big(\rho^2\big) \tag{A.3}$$

$$= d_{j,0} + \rho d_{j,1} + O\big(\rho^2\big). \tag{A.4}$$

Let $J_k = Jn_k$, where n_k is the kth component of the unit normal vector n, and using the above Taylor expansions, it follows that

$$\begin{aligned} T_{ij}J\rho &= \frac{1}{2\pi r^2}\big\{(A_1 r_i r_j + A_2\delta_{ij})r_m n_m^{(y)} + A_2 r_j n_i^{(y)} + A_3 r_i n_j^{(y)}\big\}J\rho \\ &= \frac{1}{2\pi r^2}\big\{(A_1 r_i r_j + A_2\delta_{ij})r_m J_m^{(y)} + A_2 r_j J_i^{(y)} + A_3 r_i J_j^{(y)}\big\}\rho \\ &= \frac{1}{2\pi}\left(\frac{1}{C^2\rho} + O(1)\right)\left\{\left(A_1\frac{C_i C_j}{C^2} + A_2\delta_{ij}\right)\frac{C_m}{C}J_m^{(y)} + A_2\frac{C_j}{C}J_i^{(y)} + A_3\frac{C_i}{C}J_j^{(y)} + O(\rho)\right\}. \end{aligned}$$

Now note that the smooth terms in the above formula can be expanded as

$$J_k = J_{k,0} + \rho J_{k,1} + O\big(\rho^2\big), \tag{A.5}$$

$$A_j = A_{j,0} + \rho A_{j,1} + O\big(\rho^2\big) \quad (j = 1,2,3). \tag{A.6}$$

Therefore,

$$T_{ij}J\rho = \frac{1}{2\pi}\left(\frac{1}{C^2\rho} + O(1)\right)\left\{\left(A_{1,0}\frac{C_i C_j}{C^2} + A_{2,0}\delta_{ij}\right)\frac{C_m}{C}J_{m,0}^{(y)} + A_{2,0}\frac{C_j}{C}J_{i,0}^{(y)} + A_{3,0}\frac{C_i}{C}J_{j,0}^{(y)} + O(\rho)\right\}. \tag{A.7}$$

Finally, η and each component of $\boldsymbol{\phi}$ also admit smooth expansions:

$$\eta = 1 + O\big(\rho^2\big), \tag{A.8}$$

$$\phi_j = \phi_{j,0} + \rho\phi_{j,1} + O\big(\rho^2\big). \tag{A.9}$$

By combining (A.3)–(A.9) we obtain each component of $\tilde{\mathbf{F}}_{-1}$ as follows:

$$\begin{aligned} \tilde{F}_{-1,i}(\theta) &= \sum_{j=1}^3 \frac{\phi_{j,0}}{2\pi C^2}\left\{\left(A_{1,0}\frac{C_i C_j}{C^2} + A_{2,0}\delta_{ij}\right)\frac{C_m}{C}J_{m,0} + A_{2,0}\frac{C_j}{C}J_{i,0} + A_{3,0}\frac{C_i}{C}J_{j,0}\right\} \\ &= \sum_{j=1}^3 \frac{\phi_{j,0}}{2\pi C^2}\left\{A_{2,0}\frac{C_j}{C}J_{i,0} + A_{3,0}\frac{C_i}{C}J_{j,0}\right\} \quad (i = 1,2,3), \end{aligned}$$

where the last equality follows from the fact that $C_m J_{m,0} = 0$. Similarly, for the kernel $\mathbb{W}$, the singular part

$$\tilde{F}_{-1,i}(\theta) = \sum_{j=1}^{3} -\frac{\phi_{j,0}}{2\pi C^2}\left\{A_{2,0}\frac{C_j}{C}J_{i,0} + A_{3,0}\frac{C_i}{C}J_{j,0}\right\} \quad (i = 1, 2, 3).$$

The Green tensor $\mathbb{V}$ is a hypersingular kernel, and both $\tilde{\mathbf{F}}_{-1}$ and $\tilde{\mathbf{F}}_{-2}$ do not vanish. To obtain their expressions, we follow a similar procedure. First we write explicitly each component of $\mathbb{V}$:

$$\begin{aligned} V_{ij} = \frac{-\mu}{\pi r^3}\{ & r_m n_m^{(y)}\left[(B_1 r_i r_j + B_2\delta_{ij})r_p n_p^{(x)} + B_2 r_i n_j^{(x)} + B_3 r_j n_i^{(x)}\right] \\ & + \left[B_2 r_j n_i^{(y)} + B_5 r_i n_j^{(y)}\right] r_p n_p^{(x)} + \left[B_2 r_i r_j + B_4\delta_{ij}\right] n_q^{(x)} n_q^{(y)} \\ & + \left[B_4 n_i^{(y)} n_j^{(x)} + B_6 n_j^{(y)} n_i^{(x)}\right]\}, \end{aligned}$$

where

$$\begin{aligned} B_1 &= A_1'\tau - 5A_1, \\ B_2 &= \left(A_2'\tau - 3A_2 + A_1\right)/2, \\ B_3 &= A_1 + \left(1/\left(2\alpha^2\right) - 1\right)\left(A_1'\tau + 2A_2'\tau - 6A_2\right), \\ B_4 &= A_2, \\ B_5 &= A_3'\tau - 3A_3, \\ B_6 &= A_3 + \left(1/\left(2\alpha^2\right) - 1\right)\left(A_3'\tau + 2A_2\right). \end{aligned}$$

Let

$$B_j = B_{j,0} + \rho B_{j,1} + O\left(\rho^2\right) \quad (j = 1, 2, \ldots, 6). \tag{A.10}$$

Using the expansion

$$\frac{1}{r^3} = \frac{1}{\rho^3 C^3(\theta)} - \frac{3E(\theta)}{\rho^2 C^5(\theta)} + O\left(\frac{1}{\rho}\right), \tag{A.11}$$

(A.3)–(A.5), (A.8)–(A.9), and noting that $C_m J_{m,0} = C_m n_m^{(x)} = 0$, it can be shown that

$$V_{ij} J\rho = \frac{-\mu}{\pi}\left(\frac{1}{\rho^2 C^3} - \frac{3E}{\rho C^5} + O(1)\right)\left(V_{0,ij} + \rho V_{1,ij} + O\left(\rho^2\right)\right), \tag{A.12}$$

where

$$V_{0,ij} = B_{2,0} d_{i,0} d_{j,0} J_{q,0} n_q^{(x)} + B_{4,0}\delta_{ij} J_{q,0} n_q^{(x)} + B_{4,0} J_{i,0} n_j^{(x)} + B_{6,0} J_{j,0} n_i^{(x)}$$

and

$$\begin{aligned} V_{1,ij} = {} & (d_{m,0} J_{m,1} + d_{m,1} J_{m,0})\left(B_{1,0} d_{i,0} d_{j,0} d_{p,0} + B_{2,0} d_{i,0} n_j^{(x)} + B_{3,0} d_{j,0} n_i^{(x)}\right) \\ & + (B_{2,0} d_{j,0} J_{j,0} d_{p,1} + B_{5,0} d_{i,0} d_{j,0} d_{p,1}) n_p^{(x)} + \sum_{l_i \geqslant 0}^{l_1+l_2+l_3+l_4=1} B_{2,l_1} d_{j,l_2} d_{j,l_3} J_{q,l_4} n_q^{(x)} \\ & + (B_{4,1}\delta_{ij} J_{q,0} + B_{4,0}\delta_{ij} J_{q,1}) n_q^{(x)} + (B_{4,1} J_{i,0} + B_{4,0} J_{i,1}) n_j^{(x)} + (B_{6,1} J_{j,0} + B_{6,0} J_{j,1}) n_i^{(x)}. \end{aligned}$$

Therefore, each component of $\tilde{\mathbf{F}}(\rho, \theta)$

$$\begin{aligned} \tilde{F}_i(\rho, \theta) &= \sum_{j=1}^{3} \frac{-\mu}{\pi}\left(\frac{1}{\rho^2 C^3} - \frac{3E}{\rho C^5} + O(1)\right)\left(V_{0,ij} + \rho V_{1,ij} + O\left(\rho^2\right)\right)\left(\phi_{j,0} + \rho\phi_{j,1} + O\left(\rho^2\right)\right)\left(1 + O\left(\rho^2\right)\right) \\ &= \sum_{j=1}^{3} \frac{-\mu}{\pi}\left\{\frac{V_{0,ij}\phi_{j,0}}{\rho^2 C^3} + \frac{1}{\rho}\left(-\frac{3E}{C^5} V_{0,ij}\phi_{j,0} + \frac{V_{1,ij}\phi_{j,0}}{C^3} + \frac{V_{0,ij}\phi_{j,1}}{C^3} + O(1)\right)\right\}. \end{aligned}$$

Finally, we obtain each component of $\tilde{\mathbf{F}}_{-1}$ in the following:

$$\tilde{F}_{-2,i}(\theta) = \sum_{j=1}^{3} \frac{-\mu V_{0,ij}\phi_{j,0}}{\pi C^3},$$

and

$$\tilde{F}_{-1,i}(\theta) = \frac{-\mu}{\pi}\left(-\frac{3E}{C^5}V_{0,ij}\phi_{j,0} + \frac{V_{1,ij}\phi_{j,0}}{C^3} + \frac{V_{0,ij}\phi_{j,1}}{C^3}\right).$$

Lemma A.1. *For each Green tensor,* $\tilde{\mathbf{F}}_{-1}(\theta) = -\tilde{\mathbf{F}}_{-1}(\theta+\pi)$.

Proof. For the Green tensor $\mathbb{T}$ and $\mathbb{W}$, $\tilde{\mathbf{F}}_{-1}(\theta) = -\tilde{\mathbf{F}}_{-1}(\theta+\pi)$ follows directly by noting that $C_j(\theta) = -C_j(\theta+\pi)$. For the Green tensor $\mathbb{V}$, note that

$$\begin{aligned} d_{j,0}(\theta) &= -d_{j,0}(\theta+\pi), \\ d_{j,1}(\theta) &= d_{j,1}(\theta+\pi), \\ J_{j,1}(\theta) &= -J_{j,1}(\theta+\pi), \\ B_{j,1}(\theta) &= -B_{j,1}(\theta+\pi), \end{aligned}$$

it follows that

$$V_{ij,0}(\theta) = V_{ij,0}(\theta+\pi), \qquad V_{ij,1}(\theta) = -V_{ij,1}(\theta+\pi).$$

Since $E(\theta) = -E(\theta+\pi)$, $\phi_{j,1}(\theta) = -\phi_{j,1}(\theta+\pi)$, we conclude that $\tilde{\mathbf{F}}_{-1}(\theta) = -\tilde{\mathbf{F}}_{-1}(\theta+\pi)$.

References

[1] C. Alves, T. Duong, Numerical resolution of the boundary integral equations for elastic scattering by a plane crack, Int. J. Numer. Methods Eng. 38 (1995) 2347–2371.
[2] K. Aki, P.G. Richards, Quantitative Seismology, 2nd ed., University Science Books, 2002.
[3] J. Berenger, A perfectly matched layer for the absorption of electromagnetic waves, J. Comput. Phys. 114 (1994) 185–200.
[4] N. Bleistein, J. Cohen, J. Stockwell, Mathematics of Multidimensional Seismic Imaging, Migration, and Inversion, Springer-Verlag, New York, 2001.
[5] O. Bruno, L. Kunyansky, A fast, high-order algorithm for the solution of surface scattering problems: basic implementation, tests and applications, J. Comput. Phys. 169 (2001) 80–110.
[6] O. Bruno, S. Lintner, A high-order integral solver for scalar problems of diffraction by screens and apertures in three-dimensional space, J. Comput. Phys. 252 (2013) 250–274.
[7] L. Canino, J. Ottusch, M. Stalzer, J. Visher, S. Wandzura, Numerical solution of the Helmholtz equation using a high-order Nystrom discretization, J. Comput. Phys. 146 (1998) 627–663.
[8] R. Coifman, V. Rokhlin, S. Wandzura, The fast multipole method for the wave equation: A pedestrian prescription, IEEE Antennas Propag. Mag. 35 (1993) 7–12.
[9] B. Engquist, A. Majda, Absorbing boundary conditions for the numerical simulation of waves, Math. Comput. 31 (1977) 629–651.
[10] M. Fatemi, J.F. Greenleaf, Ultrasound stimulated vibro-acoustic spectrography, Science 280 (1998) 82–85.
[11] M. Fatemi, J.F. Greenleaf, Vibro-acoustography: An imaging modality based on ultrasound-stimulated acoustic emission, Proc. Natl. Acad. Sci. 96 (1999) 6603–6608.
[12] L.B. Felsen, N. Marcuvitz, Radiation and Scattering of Waves, Prentice Hall, New York, 1973.
[13] M. Guiggiani, Formulation and numerical treatment of boundary integral equations with hypersingular kernels, in: V. Sladek, J. Sladek (Eds.), Singular Integrals in Boundary Element Methods, Computational Mechanics Publications, 1998, pp. 85–124.
[14] B. Guzina, R. Pak, A. Martínez-Castro, Singular boundary elements for three-dimensional elasticity problems, Eng. Anal. Bound. Elem. 30 (2006) 623–639.
[15] T. Ha, J. Santos, D. Sheen, Nonconforming finite element methods for the simulation of waves in viscoelastic solids, Comput. Methods Appl. Mech. Eng. 191 (2002) 5647–5670.
[16] I. Harari, S. Haham, Improved finite element methods for elastic waves, Comput. Methods Appl. Mech. Eng. 166 (1998) 143–164.
[17] S. Hestholm, B. Ruud, 3-D finite-difference elastic wave modeling including surface topography, Geophysics 63 (1998) 613–622.
[18] G. Hsiao, L. Xu, A system of boundary integral equations for the transmission problem in acoustics, Appl. Numer. Math. 61 (2011) 1017–1029.
[19] A. Kacimi, O. Laghrouche, Numerical modelling of elastic wave scattering in frequency domain by the partition of unity finite element method, Int. J. Numer. Methods Eng. 77 (2009) 1646–1669.
[20] J. Kristek, P. Moczo, Seismic-wave propagation in viscoelastic media with material discontinuities: a 3d fourth-order staggered-grid finite-difference modeling, Bull. Seismol. Soc. Am. 93 (2003) 2273–2280.
[21] Y. Liu, F. Rizzo, Hypersingular boundary integral equations for radiation and scattering of elastic waves in three dimensions, Comput. Methods Appl. Mech. Eng. 107 (1993) 131–144.
[22] P. Martin, Boundary integral equations for the scattering of elastic waves by elastic inclusions with thin interface layers, J. Nondestruct. Eval. 11 (1992) 167–174.
[23] K. Marfurt, Accuracy of finite-difference and finite-element modeling of the scalar and elastic wave equations, Geophysics 49 (1984) 533–549.
[24] P. Moczo, J. Kristek, M. Galis, P. Pazak, M. Balazovjech, The finite-difference and finite-element modeling of seismic wave propagation and earthquake motion, Acta Phys. Slovaca 57 (2007) 177–406.
[25] N. Nishimura, Fast multipole accelerated boundary integral equation methods, ASME Trans. Appl. Mech. Rev. 55 (2002) 299–324.
[26] Y.H. Pao, V. Varatharajulu, Huygens' principle, radiation conditions, and integral formulas for the scattering of elastic waves, J. Acoust. Soc. Am. 59 (1976) 1361–1371.

[27] R. Pratt, Frequency-domain elastic wave modeling by finite differences: A tool for crosshole seismic imaging, Geophysics 55 (1990) 626–636.
[28] F.J. Rizzo, D.J. Shippy, M. Rezayat, A boundary integral equation method for radiation and scattering of elastic waves in three dimensions, Int. J. Numer. Methods Eng. 21 (1985) 115–129.
[29] V. Rokhlin, Diagonal form of translation operators for the Helmholtz equation in three dimensions, Appl. Comput. Harmon. Anal. 1 (1993) 82–93.
[30] Y. Saad, M.H. Schultz, GMRES: A generalized minimal residual algorithm for solving non-symmetric linear systems, SIAM J. Sci. Stat. Comput. 7 (1986) 856–869.
[31] E. Saenger, N. Gold, S. Shapiro, Modeling the propagation of elastic waves using a modified finite-difference grid, Wave Motion 31 (2000) 77–92.
[32] F. Seron, F. Sanz, M. Kindelan, J. Badal, Finite-element method for elastic wave propagation, Commun. Appl. Numer. Methods 6 (1990) 359–368.
[33] J. Song, C. Lu, W. Chew, Multilevel fast multipole algorithm for electromagnetic scattering by large complex objects, IEEE Trans. Antennas Propag. 45 (1997) 1488–1493.
[34] J. Song, C. Lu, W. Chew, S. Lee, Fast Illinois solver code (FISC), IEEE Antennas Propag. Mag. 40 (1998) 27–34.
[35] R. Stenberg, A family of mixed finite elements for the elasticity problem, Numer. Math. 53 (1988) 513–538.
[36] M. Tong, W. Chew, Multilevel fast multipole algorithm for elastic wave scattering by large three-dimensional objects, J. Comput. Phys. 228 (2009) 921–932.
[37] J. Virieux, P-SV wave propagation in heterogeneous media: Velocity-stress finite-difference method, Geophysics 51 (1986) 889–901.
[38] C. Ying, R. Truell, Scattering of a plane longitudinal wave by a spherical obstacle in an isotropically elastic solid, J. Appl. Phys. 27 (1956) 1086–1097.